

An analytical approach to estimating aberrations in curved multilayer optics for hard x-rays:

2. Interpretation and application to focusing experiments

Ch. Morawe^{1*}, J-P. Guigay¹, V. Mocella², and C. Ferrero¹

¹ESRF, F-38043 Grenoble cedex, France

²CNR-IMM, I-80131 Napoli, Italy

*Corresponding author: morawe@esrf.fr

Abstract: Aberration effects are studied in parabolic and elliptic multilayer mirrors for hard x-rays, basing on a simple analytical approach. The interpretation of the underlying equations provides insight into fundamental limitations of the focusing properties of curved multilayers. Using realistic values for the multilayer parameters the potential impact on the broadening of the focal spot is evaluated. Within the limits of this model, systematic contributions to the spot size can be described. The work is complemented by a comparison with experimental results obtained with a W/B₄C curved multilayer mirror.

©2008 Optical Society of America

OCIS codes: (340.6720) X-ray optics, Synchrotron radiation; (340.7470) X-ray optics, X-ray mirrors; (080.2720) Geometrical optics, mathematical methods; (080.4228) Geometrical optics, non-spherical mirror surfaces; (080.1010) Geometrical optics, aberrations (global).

References and links

1. J-P. Guigay, Ch. Morawe, V. Mocella, C. Ferrero, "An analytical approach to estimating aberrations in curved multilayer optics for hard x-rays: 1. Derivation of caustic shapes," *Opt. Express* **16**, 12050-12059 (2008) and references therein.
2. H. Mimura, S. Matsuyama, H. Yumoto, S. Handa, T. Kimura, Y. Sano, K. Tamasaku, Y. Nishino, M. Yabashi, T. Ishikawa, K. Yamauchi, "Reflective optics for sub-10nm hard X-ray focusing," *Proc. SPIE* **6705**, 67050L (2007).
3. H. Mimura, S. Handa, K. Yamauchi, Department of Precision Science and Technology, Graduate School of Engineering, Osaka University, Japan (personal communication, 2008)
4. L.G. Parratt, "Surface studies of solids by total reflection of x-rays," *Phys. Rev.* **45**, 359 (1954).
5. Ch. Morawe, O. Hignette, P. Cloetens, W. Ludwig, Ch. Borel, P. Bernard, A. Rommeveaux, "Graded multilayers for focusing hard x rays below 50 nm," *Proc. SPIE* **6317**, 63170F (2006).
6. M. Schuster, H. Göbel, "Parallel beam coupling into channel-cut monochromators using curved graded multilayers," *J. Phys. D: Appl. Phys.*, **28**, A270 (1995).
7. Ch. Morawe, P. Pecci, J-Ch. Peffen, E. Ziegler, "Design and performance of graded multilayers as focusing elements for x-ray optics," *Rev. Sci. Instrum.* **70**, 3227 (1999).

1. Introduction

Recently, analytical ray-tracing techniques were developed to study the impact of angular variations and beam penetration effects on curved Reflective Multilayers (RMLs) [1]. Both parabolic and elliptic focusing geometries were investigated (s. Fig. 1). For the sake of simplicity the whole ML stack is represented by only two interfaces filled with a medium of average optical index $n = 1 - \delta$. Figure 2 illustrates how the rays propagate upon reflection and transmission through the RML. For a detailed description of the formalism used in the following the reader is referred to [1].

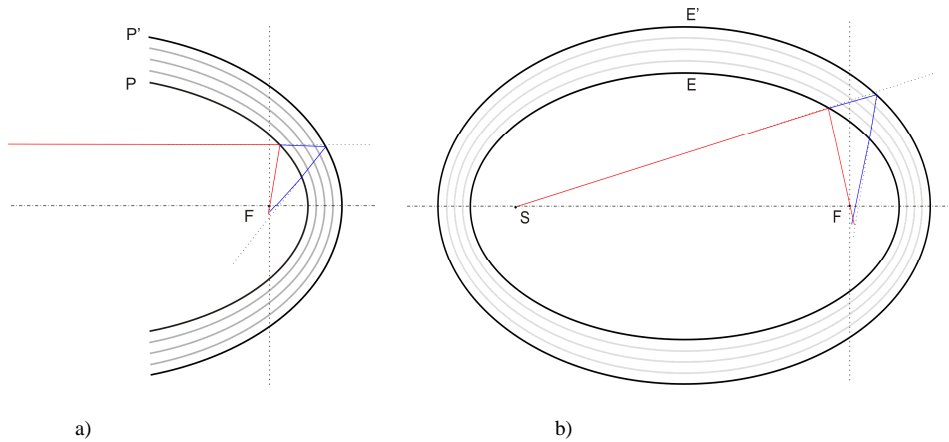


Fig. 1. Basic focusing geometries of parabolic (a) and elliptic (b) RMLs. Red lines indicate rays reflected from the upper surface (P or E). Blue lines represent rays undergoing a reflection at the deeper interface (P' or E'). The rays are refracted at each passage through the upper surface.

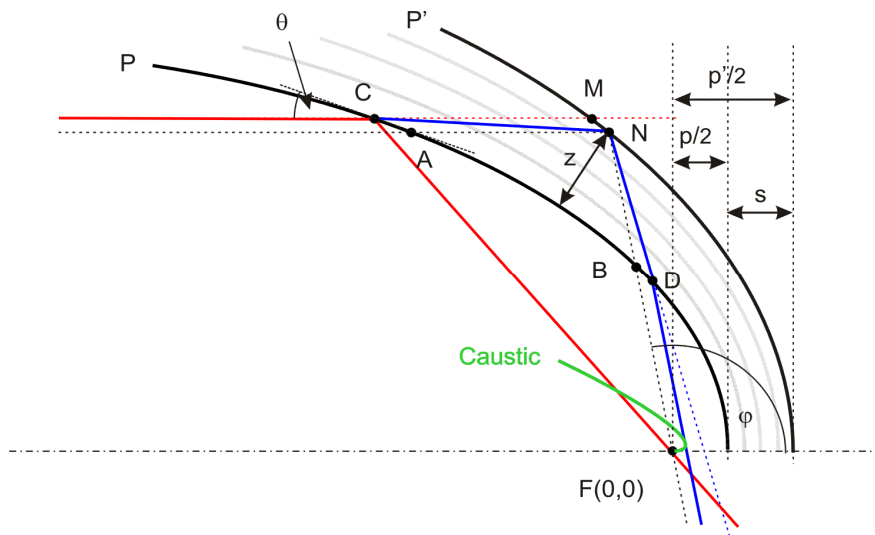


Fig. 2. Close-up of the region of interest of Figs. 1. For simplicity's sake, only the parabolic approximation is shown. The red solid line shows a ray reflected from the upper ML surface reaching the ideal focus F. The blue solid line indicates a ray that is first refracted when crossing P in point C, then reflected in point N on P', and again refracted when crossing P in point D. The green solid line represents the resulting envelope of all rays reflected from P'. The polar angle ϕ is defined by the virtual ray reflected in point N without refraction in the ML medium (broken line). The dimensions are not to scale.

2. Parametric equations for the caustic curve

2.1 Parabola

The analytical derivation has been done for two parabolas (P) and (P') having the same focus F (0,0) and vertices in $(p/2,0)$ and $(p/2+s,0)$. The parabolas are illuminated by parallel beams corresponding to a plane wave with infinite source distance. The emerging rays were traced to first order in δ , leading to the parametric equations of the caustic:

$$\begin{aligned} x(t) &= \delta \cdot s \cdot (1 + s/p) \cdot (1 + 6 \cdot t^2 - 3 \cdot t^4) \\ y(t) &= \delta \cdot s \cdot (1 + s/p) \cdot 8 \cdot t^3 \end{aligned} \quad (1)$$

where $t = \tan(\varphi/2)$. The physical meaning of s is linked to the local extinction depth $z(\theta)$ of the multilayer and will be explained in more detail in section 4. For $\delta=0$ or $s=0$ this caustic coincides with the ideal focus $F(0,0)$.

2.2 Ellipse

The treatment for a finite distance from the source and a cylindrical wave-front requires two confocal ellipses with foci in S and F and different eccentricities e and e' , respectively. The derivation leads to a set of extended algebraic equations. For eccentricities close to 1, however, the solutions for the caustic converge to the parabolic case (1) [1].

For the sake of simplicity, the following discussion will be based on Eq. (1).

3. Interpretation of the results

Two fundamental cases may be considered in order to interpret Eq. (1):

1. Aberrations due to a single interface illuminated at variable angles of incidence where $\delta = \text{const}$ and $s = \text{const}$, while t ranges from t_1 to t_2 , i.e. the mirror edges.
2. Aberrations originating from interfaces at variable penetration depths at a given angle of incidence where $t = \text{const}$, while s ranges from 0 (top surface) to s_{max} , given by the extinction depth z of the multilayer.

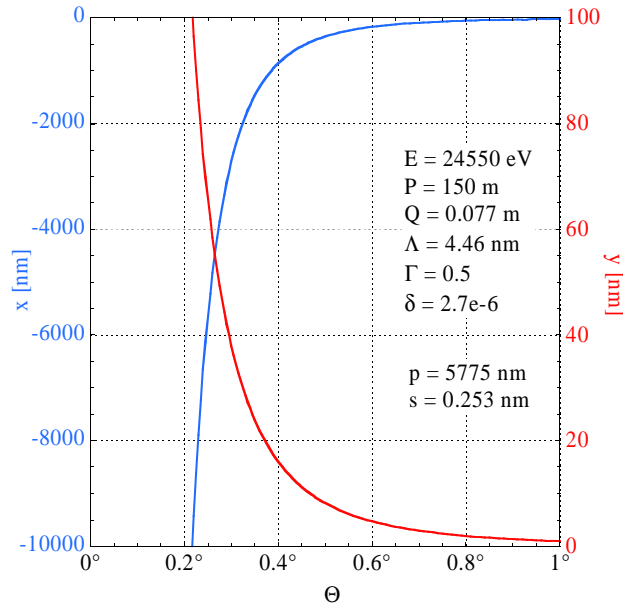


Fig. 3. Caustic curves x (blue) and y (red) as a function of the grazing incident angle θ .

3.1 Single interface aberrations

The angular dependence of Eq. (1) is depicted in Fig. 3 for positive polar angles φ and for a set of parameters typical for hard x-ray focusing experiments. Here, E is the photon energy, P the source-to-RML distance, Q the RML-to-image distance, Λ the d-spacing, and Γ the filling

factor of the multilayer structure (see section 6 for more details). For very small angles of incidence θ , both x and y diverge. The displacement in x is negative with respect to the beam direction and about two orders of magnitude stronger than in y direction. Figure 4 shows the caustic curve $y(x)$ and the angle of incidence $\theta(x)$ in a functional form along the optical axis and for the same parameters as in Fig. 3. Only the branch for positive polar angles ϕ is plotted.

The behaviour close to the ideal focal point $F(0,0)$ is illustrated in the insert of Fig. 4. The caustic is indicated in red, the angles in blue. The small zero x -offset of

$$x(\theta = \pi/2) = \delta \cdot s \cdot (1 + s/p)$$

at normal incidence can be confirmed using Gaussian optics and the classical conjugation formulas on a sequence of the related optical surfaces. Obviously, the effect disappears for $\delta = 0$ or $s = 0$.

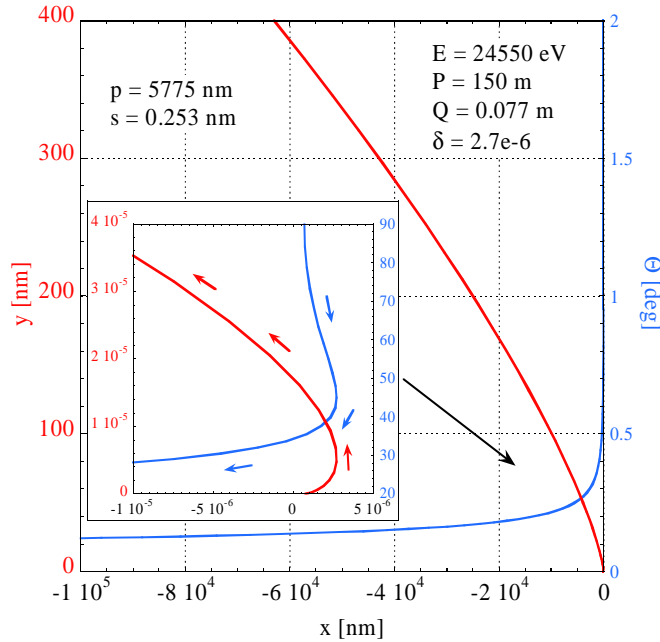


Fig. 4. Positive branch of the caustic curve $y(x)$ (red line) and corresponding grazing incidence angle $\theta(x)$ (blue line) for the same set of parameters as in Fig. 3. The insert zooms into the zone around the ideal focus and the corresponding angles of incidence.

3.2. Variable penetration

Case 2 can be approximated analytically by Eq. (1). At a given position on a curved mirror under grazing beam incidence, the polar angle variation due to variable beam penetration is of the order of

$$\frac{\Delta\phi}{\phi} \approx 10^{-6}$$

In the present calculation, t can thereby be considered to be constant along the depth and $s \ll p$ for all s values. Eliminating the corresponding terms in Eq. (1) one obtains

$$y(x) = \frac{8 \cdot t^3}{1 + 6 \cdot t^2 - 3 \cdot t^4} \cdot x \quad (2)$$

At a given angle of incidence the caustic can therefore be approximated by a straight line through the ideal focus. In other words, both s and δ essentially amplify the angular effect at a given location on a curved ML mirror.

4. Graphical representation of the caustic area

It is helpful to calculate the trajectories of some rays for a given penetration parameter s . The corresponding Eqs. (2) and (3) in reference [1] can be simplified. For small grazing angles one obtains at the intersection points $X(Y=0)$ with the optical axis and $Y(X=0)$ with the focal plane

$$\begin{aligned} X(Y=0) &\approx \delta \cdot s \cdot (1 + 2 \cdot t^2 + t^4) \approx \delta \cdot s \cdot t^4 \\ Y(X=0) &\approx 2 \cdot \delta \cdot s \cdot (2 \cdot t + t^3) \approx 2 \cdot \delta \cdot s \cdot t^3 \end{aligned} \quad (3)$$

Note that Eqs. (1) and (3) have a very similar structure and their leading terms go with the same power in t . Figure 5 shows how the rays are located with respect to the caustic. Each ray (arrows) is tangential to the caustic curve (black line) at the point where the latter intersects the line corresponding to the local grazing angle (broken lines). The intersection points with the focal plane and with the optical axis are plotted in Fig. 6 for the same parameter set (solid lines). For comparison, the results of an exact numerical calculation are added (broken lines). As expected, the curves are in very good agreement except for the region near the critical angle, where the linear approximation used to derive Eqs. (1) and (3) fails. It is interesting to note that, apart from a small scaling factor, these findings are similar to calculations done at Osaka University using a ray tracing computer program [2, 3].

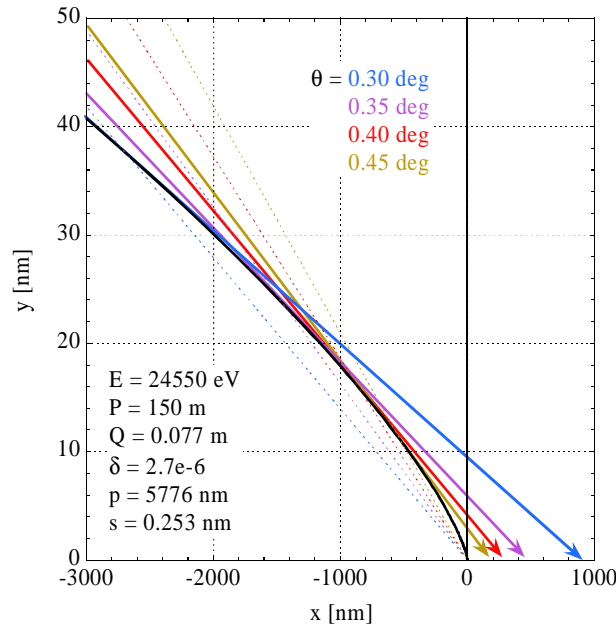


Fig. 5. Family of rays (coloured arrows), emerging from a curved RML with constant penetration parameter s but variable grazing angles. The black curve is the corresponding caustic. Each broken line intersects the caustic at a given angle of incidence (see colour coded list). By definition, each ray is the tangent line to the caustic at the respective intersection point.

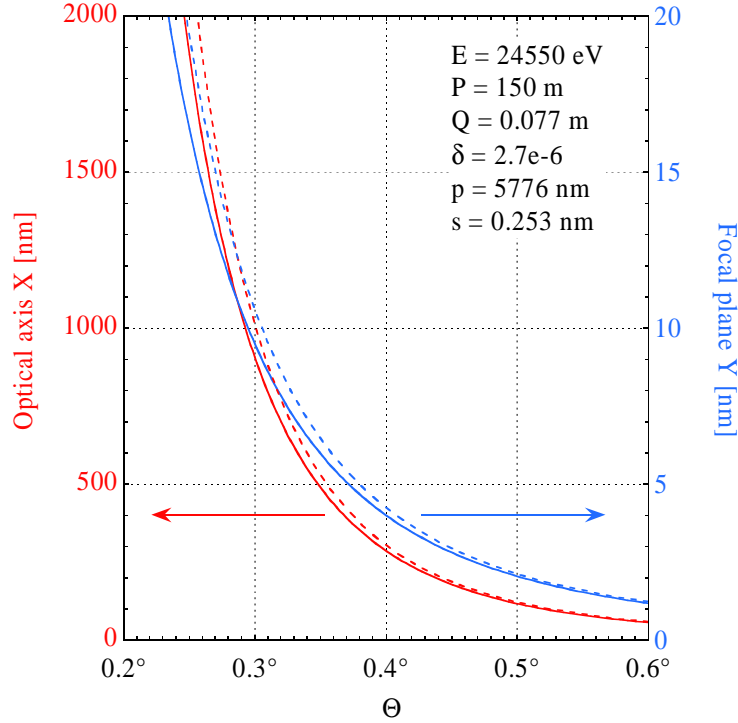


Fig. 6. Intersection points of the emerging rays with the optical axis (red) and with the focal plane (blue) as a function of the grazing angle. Solid curves were derived from Eq. (3). Broken lines indicate exact numerical calculations. The data set corresponds to the case shown in Fig. 5.

In a real RML both angular and penetration effects occur at the same time and s and θ are not independent variables, but are linked through the angle-dependent penetration. The relation between the local grazing angle θ and the local d-spacing Λ of a curved RML is given by the corrected Bragg equation

$$m \cdot \lambda = 2 \cdot \Lambda \cdot \sqrt{n^2 - \cos^2 \theta} \quad (4)$$

where m denotes the reflection order and n the average optical index in the stack. The local penetration depth $z(\theta)$ varies along the selected interface P' , which is by definition a $s = \text{const.}$ curve. The penetration depth is typically a multiple of Λ . For a given set of θ and $z(\theta)$, one may approximate s by projecting the illuminated zone of the RML to the vertex of the parabola

$$2 \cdot s \cdot \sqrt{n^2 - \cos^2(\pi/2)} \approx 2 \cdot z(\theta) \cdot \sqrt{n^2 - \cos^2 \theta} \quad (5)$$

giving

$$s \approx z(\theta) \cdot \sqrt{n^2 - \cos^2 \theta} \approx z(\theta) \cdot \sqrt{\sin^2 \theta - 2 \cdot \delta} \approx z(\theta) \cdot \sin \theta \approx \text{const.} \quad (6)$$

Focusing setups at synchrotron beamlines are characterized by the source distance P , the image distance Q , and the angle of incidence θ . P , Q , and θ are usually defined at the centre of the optical element. The principal axes of the corresponding ellipse can then be calculated using

$$\begin{aligned}
a &= (P+Q)/2 \\
b &= \sqrt{P \cdot Q} \cdot \sin \theta \\
c &= \sqrt{a^2 - b^2}
\end{aligned}
\tag{7}$$

Due to the grazing incidence angles the ellipse is very eccentric ($a \gg b$) and can be approximated by a parabola using the equations

$$a - c = a - \sqrt{a^2 - b^2} = \frac{p}{2} \tag{8}$$

where p now denotes the parabola parameter in the normal form

$$y^2 = 2 \cdot p \cdot |x|. \tag{9}$$

To extract shape and dimensions of the caustic area for a given RML mirror, dedicated numerical calculations for particular flat MLs were carried out, and are presented in section 5.

5. Influence of the multilayer d-spacing

To understand the influence of the ML d-spacing Λ on the caustic the following approach is proposed. For a given d-spacing the bi-layer number N_C from the surface to the interface under investigation was chosen to give $1-1/e$ times the maximum possible peak reflectivity R_{MAX} , assuming that deeper interfaces do not significantly contribute to the total reflectivity response.

$$R(N_C) = (1 - 1/e) \cdot R_{MAX} \tag{10}$$

The numbers as well as the exact grazing angles θ were calculated numerically using the Parratt formalism [4] for the x-ray reflectivity of flat layered structures. The corresponding values of the penetration depth $z = N_C \cdot \Lambda$ were then used to calculate s and p for each d-spacing, using Eqs. (6)-(8). Tab.1 summarizes the values for a W/B₄C multilayer with mass densities $\rho(\text{B}_4\text{C}) = 2.3 \text{ g/cm}^3$ and $\rho(\text{W}) = 16.3 \text{ g/cm}^3$ and with interface widths of $\sigma = 0.3 \text{ nm RMS}$. Similar data sets were calculated for variable interface widths from 0 to 0.3 nm RMS.

Table 1. ID19 W/B₄C multilayer characteristics for various d-spacings.

Λ [nm]	θ	N_C	t	z [nm]	s [nm]	b [mm]	p [nm]
1.50	0.973°	163	58.88	244.5	4.113	57.71	44380
2.00	0.735°	67	77.95	134.0	1.691	43.60	25325
3.00	0.499°	24	114.8	72.00	0.6043	29.60	11673
4.00	0.382°	13	145.0	52.00	0.3250	22.66	6841
4.46	0.351°	10	163.2	44.60	0.2528	20.82	5776
5.00	0.312°	8	183.6	40.00	0.1970	18.51	4563
6.00	0.266°	5	215.4	30.00	0.1206	15.78	3317
7.00	0.236°	4	242.8	28.00	0.0952	14.00	2611

6. Chromaticity

Equation (3) offer the opportunity to estimate chromatic aberration in curved RMLs and to compare them with other types of focusing elements. The refractive decrement δ is energy dependent. For hard x-rays and far away from absorption edges δ exhibits the following energy dependence:

$$\delta \sim 1/E^2 \quad (11)$$

The change of the focal distance due to dispersive effects can be approximated by the first of Eq. (3). Keeping the focusing geometry constant, it follows

$$f = f_0 + \Delta f = f_0 + G/E^2, \quad (12)$$

where G varies only slowly with energy through s . The dispersion can therefore be written as

$$\left| \frac{df}{dE} \right|_{RML} = 2 \cdot \frac{\Delta f}{E} \quad (13)$$

It is instructive to compare this result with the cases of Fresnel Zone Plates (FZP) and Compound Refractive Lenses (CRL)

$$\left| \frac{df}{dE} \right|_{FZP} = \frac{f}{E} \quad (14)$$

$$\left| \frac{df}{dE} \right|_{CRL} = 2 \cdot \frac{f}{E} \quad (15)$$

The linear dependence of Δf on δ may appear somewhat artificial and caused by the linear approximation on which the model is based. Indeed, higher order terms cannot be excluded, though the respective coefficients are very small. The essential point is, however, the fact that δ acts on Δf and not on f .

To calculate the energy bandwidth that can be tolerated for a given focusing geometry, one can require that the chromatic blurring D_{chrom} does not exceed the diffraction limit D_{diff} of the setup.

$$D_{tot}^2 = D_{diff}^2 + D_{chrom}^2 \leq 2 \cdot D_{diff}^2 \quad (16)$$

D_{diff} and D_{chrom} are given by the following expressions

$$D_{diff} = \frac{0.44 \cdot \lambda}{NA} \quad (17)$$

$$D_{chrom} = 2 \cdot NA \cdot df \quad (18)$$

for rectangular apertures, where NA is the numerical aperture of the optical element. Inserting expressions (17) and (18) into Eq. (16) one obtains

$$df = \frac{D_{diff}^2}{0.88 \cdot \lambda} = \frac{D_{tot}^2}{1.76 \cdot \lambda} \quad (19)$$

Table 2 summarizes the resulting expressions for the energy bandwidth referring to all three types of optical elements as derived from Eqs. (13)-(15) and (19).

Table 2. Comparison of the tolerated energy bandwidth of various optical elements.

	FZP	CRL	RML
$\frac{dE}{E}$	$\frac{D_{tot}^2}{1.76 \cdot f \cdot \lambda}$	$\frac{D_{tot}^2}{3.52 \cdot f \cdot \lambda}$	$\frac{D_{tot}^2}{3.52 \cdot \Delta f \cdot \lambda}$

The physical background of the different impact on the chromaticity is clear. For FZPs and CRLs the phase shift induced by the optical elements is at the origin of their focusing properties and chromaticity, and therefore unavoidable. In the case of RMLs, however, it is only a parasitic effect that should be reduced as much as possible.

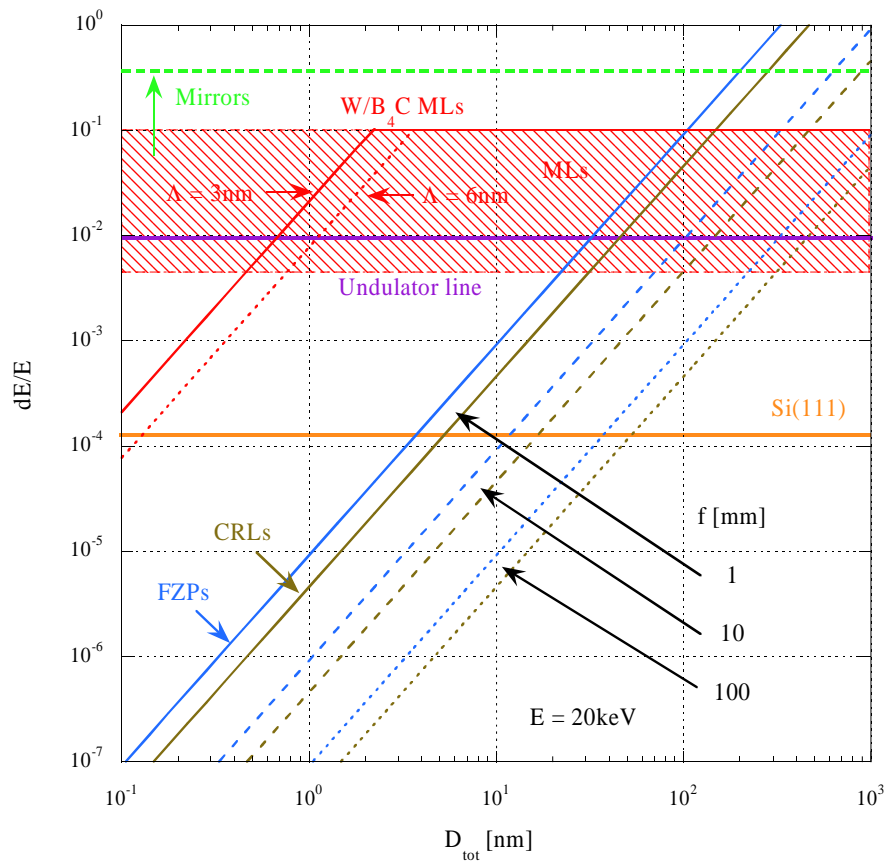


Fig. 7. Chromatic blurring of different x-ray optical elements and bandwidth of hard x-ray sources and monochromators at 20 keV. Straight lines indicate RMLs (red), FZPs (blue), and CRLs (brown). The chromaticity of FZPs and CRLs is shown for three different focal lengths (1 mm, 10 mm, and 100 mm). For the RMLs two W/B₄C structures with periods of 3 nm and 6 nm are shown. The bandwidths of a typical undulator source (purple line), of a Si(111) reflection (orange line), and of a ML monochromator (shaded red area) are added. Total reflection mirrors are indicated by the green broken line.

Figure 7 illustrates the chromatic blurring at 20 keV and compares it with the bandwidth of typical hard x-ray sources and monochromators. Straight lines indicate RMLs (red), FZPs (blue), and CRLs (brown). The chromaticity of FZPs and CRLs depends intrinsically on the focal distance f , as shown for three different cases (1 mm, 10 mm, and 100 mm). For the RMLs two W/B₄C structures with periods of 3 nm and 6 nm, respectively, are shown. The bandwidths of a typical undulator source (purple line), of a Si(111) reflection (orange line), and of a ML monochromator (shaded red area) are also included. Total reflection mirrors are indicated by the green broken line.

Considering presently achievable focal spots sizes of about 100 nm, FZPs and CRLs can be operated with a Si(111) monochromator, for very short focal lengths (<10 mm) even with a full undulator line. RMLs are limited only by their intrinsic bandwidth of several percent. However, when going to focal spots of the order of 10 nm or below, declared aim of most 3rd generation synchrotron sources, FZPs and CRLs would require monochromators with an energy resolution better than 10^{-4} , except for $f < 10$ mm. RMLs could still accept a full undulator line down to spots of less than 1 nm. The advantage would not only be higher photon flux on the sample. Scattering from nano-objects generally benefits from a broad energy band-pass.

Figure 7 does not describe the absolute focusing limit of the respective element, which is essentially given by Eq. (17). It rather helps understanding better the matter by highlighting the influence of chromatic aberrations and gives guidance on the selection of the appropriate optical element for a given situation.

7. Comparison with experimental data

Focusing experiments were carried out on the ESRF insertion device beamline ID19, where a focal line with 45 nm FWHM was achieved [5]. A dynamically bent [W/B₄C]₂₅ ML mirror was used under the following conditions:

$$E = 24550 \text{ eV}, \lambda = 0.05051 \text{ nm}$$

$$\Lambda = 4.457 \text{ nm}$$

$$\delta = 2.7 \cdot 10^{-6}$$

The ideal surface figure was assumed to be elliptic with the following values (referring to the centre of the beam footprint on the mirror):

$$P = 150018.2 \text{ mm} \quad \text{or equivalent} \quad a = 75047.5 \text{ mm}$$

$$Q = 76.9 \text{ mm} \quad b = 20.82 \text{ mm}$$

$$\theta = 0.351^\circ \quad c = 75047.5 \text{ mm}$$

The incident angle range along the beam footprint was $\theta = 0.334^\circ \dots 0.371^\circ$. This very eccentric ellipse can be approximated by a parabola using Eq. (8). The corresponding ML characteristics are given in Table 1 (bold printed data row).

Based on the general interpretation in the previous section, the particular case of the ID19 experiment is illustrated in Fig. 8. It shows the positive branch of the caustic area spanned by the angular variation along the RML combined with the depth variation of the reflecting interfaces. The upper limit is estimated via the penetration depth z (see Table 1). It basically corresponds to a cone with its tip on the ideal focus stretching up to values of $x = -1.5 \mu\text{m}$ and $y = 24 \text{ nm}$. The opening of the cone is limited to $\Delta y < 3 \text{ nm}$.

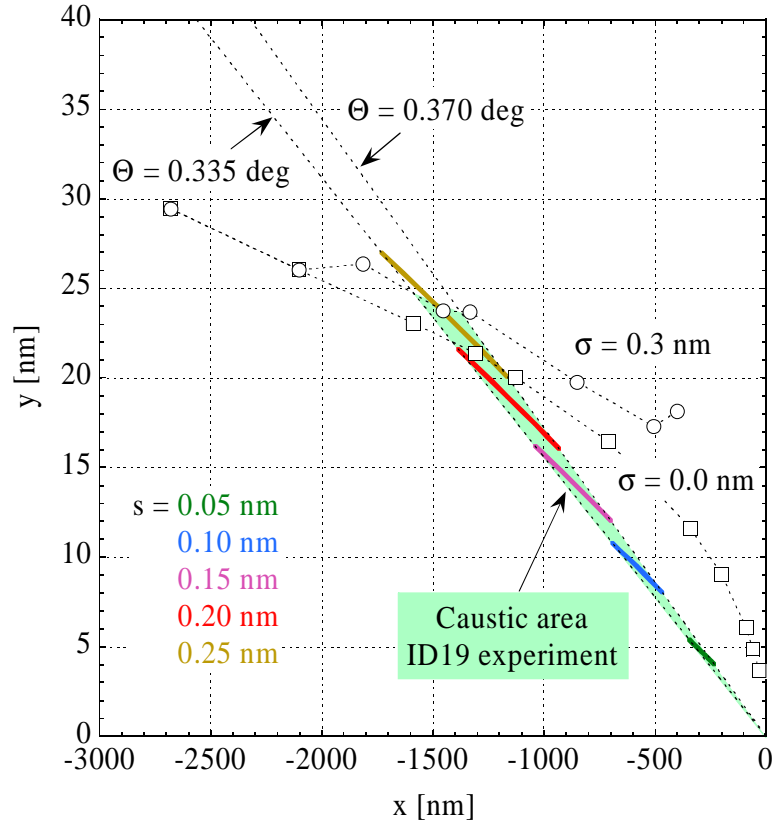


Fig. 8. Positive branch of the caustic area (green triangle) spanned by both the angular and the depth variation. The intersections with the $y(x(\theta))$ curves are plotted for $s = 0.05 \dots 0.25$ nm (thick lines in colour). The limiting $y(x(s))$ curves are the broken lines. The open symbols indicate the upper limit due to the penetration effect for various ML d-spacings.

A comparison of the caustic area with the expected diffraction waist from the aperture of the RML is shown in Fig. 9. In the present case, the diffraction limited spot size is about 35 nm FWHM. The measured size was 45 nm FWHM. It is evident that the spot size is dominated by diffraction effects and additional mirror imperfections. Figure 9 also shows that the caustic is oriented almost parallel to the principal beam direction. The caustic slope m_C can be approximated from Eq. (2) and the average slope of the incoming beam m_B can be expressed by

$$y = -x \cdot \tan 2\theta \quad (20)$$

Here, θ has to be taken as the mean angle of incidence on the RML. Comparing Eqs. (2) and (20) it turns out that, for grazing incidence, the respective slopes follow the simple relation

$$\frac{m_C}{m_B} \approx \frac{4}{3}. \quad (21)$$

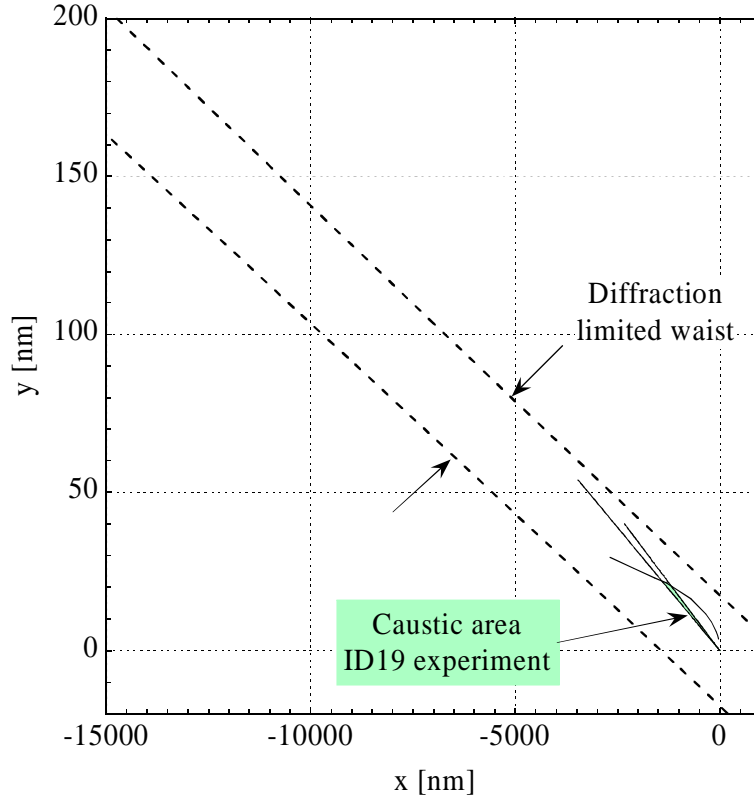


Fig. 9. Large scale view on the zone near the ideal focus. The broken lines show the beam waist as expected due to diffraction from the aperture of the RML compared with the caustic area. The graph illustrates the characteristic tilt of the caustic with respect to the principal beam direction.

This misalignment causes a contribution dy to aberrations in y caused by the extended caustic in the x -direction. It can be derived by calculating the difference of the two slope functions at a given value on the x -axis. Using Eqs. (20) and (21) one finds

$$dy = (m_c - m_B) \cdot x = -1/3 \cdot \tan 2\theta \cdot x \quad (22)$$

Inserting the first Eq. (1) into (22) and considering only grazing incidence, one obtains

$$dy = \delta \cdot s \cdot (1 + s/p) \cdot 2 \cdot t^3 = 1/4 \cdot y(t) \quad (23)$$

Within the given approximations there is obviously a direct relation between the y -position of the caustic and its contribution to the blurring in the image plane, being caused by its inclination with respect to the incoming beam. In the present geometry the effect amounts to about 6 nm and Eq. (23) shows that it drops while increasing the angle of incidence.

It is evident from Fig. 9 that the available experimental data is insufficient to confirm the presence of the caustic zone as derived within the analytical framework of this study. RML-based focusing optics with a diffraction limit below 10 nm would be needed. So far, such devices are not available, but strong efforts are underway to develop the required technologies [2].

8. Summary and outlook

Thanks to its simplified approach, the analytical model described here offers a general insight into the focusing performance of RMLs in the hard x-ray range. Assuming perfect ellipses or parabolas, the expected aberrations from the ideal focus are in the micrometer range along the optical axis and nanometric normal to it. Increasing angles of incidence improve the focusing performance. Chromatic aberrations are present yet by orders of magnitude smaller than in other optical elements.

It is known that the optimum shapes of focusing RMLs are not perfect ellipses or parabolas (except for the upper surface). In the past it has been a general practice to assume that RMLs have to fulfil Bragg's law locally [6] in order to provide constructive interference for the same photon energy at any point along the optical element. The ML d-spacings and consequently the interface spatial positions change as the optical indices differ from unity. Unfortunately, these modifications do not lead to simple mathematical expressions like a perfect ellipse or parabola.

One may expect that the present analytical approach overestimates aberration due to refraction and that the design of an optimized structure allows a significant improvement of the focal spot size [2].

A coherent treatment of the problem certainly requires the use of wave-optical theories. The electromagnetic wave propagation inside a curved ML depends on the local change of the optical density between neighbouring layers and on multiple reflections within the stack. Graded and/or rough interfaces occur in real devices and will have to be taken into account. Future work will have to focus on both the study of appropriate wave-optical models and on the development of enabling technologies to carry out focusing experiments on the nanometer scale.